Experimental Demonstration of Spintronic Broadband Microwave Detectors and Their Capability for Powering Nanodevices

Bin Fang, Mario Carpentieri, Steven Louis, Vasyl Tiberkevich, Andrei Slavin, Ilya N. Krivorotov, Riccardo Tomasello, Anna Giordano, Hongwen Jiang, Jialin Cai, Yaming Fan, Zehong Zhang, Baoshun Zhang, Jordan A. Katine, Kang L. Wang, Pedram Khalili Amiri, Giovanni Finocchio, and Zhongming Zeng

Phys. Rev. Applied **11**, 014022 — Published 10 January 2019

DOI: 10.1103/PhysRevApplied.11.014022

Experimental Demonstration of Spintronic Broadband Microwave Detectors and Their Capability for Powering Nanodevices

Bin Fang,[1] Mario Carpentieri,[2] Steven Louis,[3] Vasyl Tiberkevich,[4] Andrei Slavin,[4] Ilya N. Krivorotov,[5] Riccardo Tomasello,[6] Anna Giordano,[7] Hongwen Jiang,[8] Jialin Cai,[1] Yaming Fan,[1] Zehong Zhang,[1] Baoshun Zhang,[1] Jordan A. Katine,[9] Kang L. Wang,[10] Pedram Khalili Amiri,[10,11] Giovanni Finocchio,[7,*] and Zhongming Zeng[1]

[1] *Key Laboratory of Nanodevices and Applications, Suzhou Institute of Nano-tech and Nano-bionics, Chinese Academy of Sciences, Ruoshui Road 398, Suzhou 215123, P. R. China*

[2] *Department of Electrical and Information Engineering, Polytechnic of Bari, Bari 70125, Italy*

[3] *Department of Electrical and Computer Engineering, Oakland University, Rochester, Michigan 48309, USA*

[4] *Department of Physics, Oakland University, Rochester, Michigan 48309, USA*

[5] *Department of Physics and Astronomy, University of California, Irvine, California 92697, USA*

[6] *Institute of Applied and Computational Mathematics, FORTH, GR-70013, Heraklion-Crete, Greece*

[7] *Department of Mathematical and Computer Sciences, Physical Sciences and Earth Sciences, University of Messina, Messina 98166, Italy*

[8] *Department of Physics and Astronomy, University of California, Los Angeles, California 90095, USA*

[9] *Western Digital, San Jose, California 95138, USA*

[10] *Department of Electrical and Computer Engineering, University of California, Los Angeles, California 90095, USA*

[11] *Department of Electrical Engineering and Computer Science, Northwestern University, Evanston, Illinois 60208, USA*

(Received 28 June 2018; revised manuscript received 10 November 2018; published XX XX 2019)

Nonlinear dynamics has been the key ingredient to improve the performance, in terms of sensitivity, of biased resonant spintronic diodes beyond their semiconductor counterparts. We experimentally demonstrate a nonlinear regime broadband detection for nanoscale spintronic diodes (NSD) where the rectification properties are independent of the input microwave frequency, and compare the device performance with the state of the art Schottky diode for low-power rectification. This regime is achieved in magnetic tunnel junctions with a canted magnetization of the free layer. We further show that the developed NSD provides sufficient dc voltage to supply a low-power nanodevice – a black phosphorus photosensor. Our results could pave the way for using spintronic detectors as building blocks for self-powered nanosystems, such as implantable biomedical devices, wireless sensors, and portable electronics.

DOI: 10.1103/PhysRevApplied.0.XXXXXX

I. INTRODUCTION

Energy-harvesting technologies offer a promising approach to capture energy from ambient sources, such as vibration, heat, and electromagnetic waves. Spintronic technologies, which use both the charge and spin of electrons, are a viable alternative for the development of energy-efficient electronic systems, e.g., magnetic sensors, memory, oscillators, and detectors [1–6]. In particular, the discovery of the spin Seeback effect has given spintronics an approach to energy-harvesting technologies via the idea of thermoelectric power generators [7,8]. In addition, biased resonant spintronic diodes exhibit sensitivities (defined as output rectified voltage over input microwave power) larger than that of the Schottky diodes [9–11].

The starting point of this work is the theoretical prediction that spintronic diodes, biased with a large enough out-of-plane field, can act as broadband detectors and hence, can be used for electromagnetic energy harvesters [12]. First of all, we figure out an approach to have a bias-free broadband detection. This result is accomplished by fine-tuning the magnetic anisotropy [13,14] of the free layer of a magnetic tunnel junction (MTJ) to stabilize an equilibrium magnetization directed along an oblique easy axis (canted magnetization). Finally, we show that nanoscale

*gfinocchio@unime.it

spintronic diodes (NSD) are capable of powering a black phosphorus (BP) photosensor [15–17].

II. BROADBAND SPINTRONIC DIODE

A. Working principle

The two operational principles of NSDs are illustrated in Fig. 1(a). In a regular regime, a weak ac current will be spin polarized as it passes through a fixed magnetic layer and enters the free layer of a MTJ. This spin-polarized current excites a small-amplitude magnetization precession [Fig. 1(a), trajectory in red], which then creates a rectification voltage V_{dc} across the MTJ that is highest near the ferromagnetic resonance (FMR) frequency [6,18–22]. On the other hand, the broadband detection is based on the excitation of a large-amplitude magnetization precession [Fig. 1(a), trajectory in blue] giving rise to the same rectification voltage V_{dc} over a broad frequency range.

B. Device realization and characterization

The MTJs are fabricated with a continuous multilayer thin-film stack composed of PtMn (15)-$Co_{70}Fe_{30}$ (2.3)-Ru (0.85)-$Co_{40}Fe_{40}B_{20}$(2.4)-MgO(0.8)-$Co_{20}Fe_{60}B_{20}$ (1.65) (thicknesses in nm) [Fig. 1(b)]. The synthetic antiferromagnetic polarizer has an in-plane magnetization and it is exchange-biased with PtMn. The free layer is composed of $Co_{20}Fe_{60}B_{20}$ while the MgO tunnel barrier ensures a high magnetoresistance effect [23,24]. The perpendicular magnetic anisotropy (PMA) in the $Co_{20}Fe_{60}B_{20}$-MgO bilayer is caused by an interfacial effect that arises from the hybridization between the O (from the MgO) and Fe (from the $Co_{20}Fe_{60}B_{20}$) orbitals, and can be controlled by the $Co_{20}Fe_{60}B_{20}$ composition and thickness of the free layer [13,14,25,26]. In other words, below a critical thickness, the free layer easy axis is out-of-plane. The devices studied here are designed to have a free layer thickness near, but below, this critical value, so that the PMA field almost compensates for the out-of-plane demagnetizing field ($K_1 - 0.5\mu_0 M_S^2 \approx 0$, where K_1 is the first-order anisotropy coefficient, μ_0 is the vacuum permeability, and M_S is the saturation magnetization). In this scenario, the second-order magnetic anisotropy plays a crucial role in controlling the magnetization configuration, even though K_2 (K_2 is the second-order anisotropy coefficient) is smaller than K_1 by about one order of magnitude (see also Supplementary Note 1 for the expression of the anisotropy fields and for more details about the micromagnetic model [27]).

The magnetic multilayer film stack is patterned into elliptical nanopillars by using electron-beam lithography and ion milling techniques. The representative results presented here are from a device with dimensions of 150×50 nm^2, while similar results are obtained on a variety of samples with other dimensions. All data are gathered at room temperature.

In order to evaluate the PMA in the studied MTJ, we perform the spin-torque FMR (ST FMR) measurement under various external in-plane magnetic fields at zero dc bias voltage and low input power. Figure 2(a) shows the rectified dc voltages of the device presented in the main text as a function of the microwave frequency for different in-plane magnetic fields. The ST FMR spectra can be well fitted by a sum of symmetric and antisymmetric Lorentzians with identical resonance frequencies f_0 [21]. The first- (H_{k1}) and second-order (H_{k2}) perpendicular anisotropy fields can be deduced from the magnetic field dependence of the resonance frequency f_0 [21]. The values of H_{k1} and H_{k2} are estimated to be 11 720 and 640 Oe, respectively [Fig. 2(b)]. FMR data suggest that the equilibrium configuration is a single domain state with a quasi-uniform magnetic state. If multiple domains existed, multiple peaks would be expected in the FMR [28].

We also characterize the resistance of the NSD as a function of the magnetic field applied either parallel to the ellipse major axis ($H_{\parallel}$) or perpendicular to the sample plane ($H_{\perp}$) [see Figs. 2(c) and 2(d)]. The hysteresis observed for the out-of-plane field scan indicates that the PMA is still larger than the out-of-plane demagnetizing

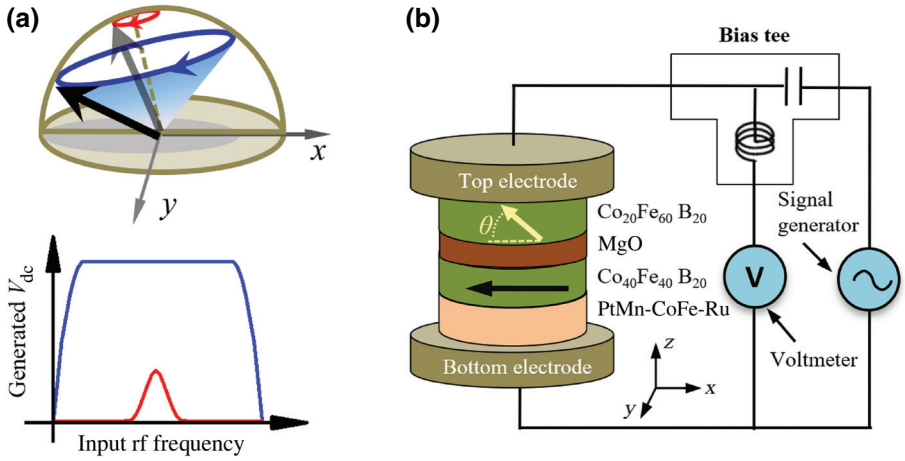

FIG. 1. (a) Schematic image of the magnetization precession in the nanomagnet. Under a rf current, the free-layer magnetization rotates around from the initial state, causing a small (large) dc voltage if we are dealing with resonant (broadband) NSD. (b) Spintronic diode devices and circuit schematics are used for diode-effect measurements. The device is based on a MTJ with an in-plane magnetized polarizer layer and a free layer with canted magnetization, separated by an MgO tunnel barrier. The generated voltage (V_{dc}) is measured by a nanovoltmeter in response to a rf current from a signal generator.

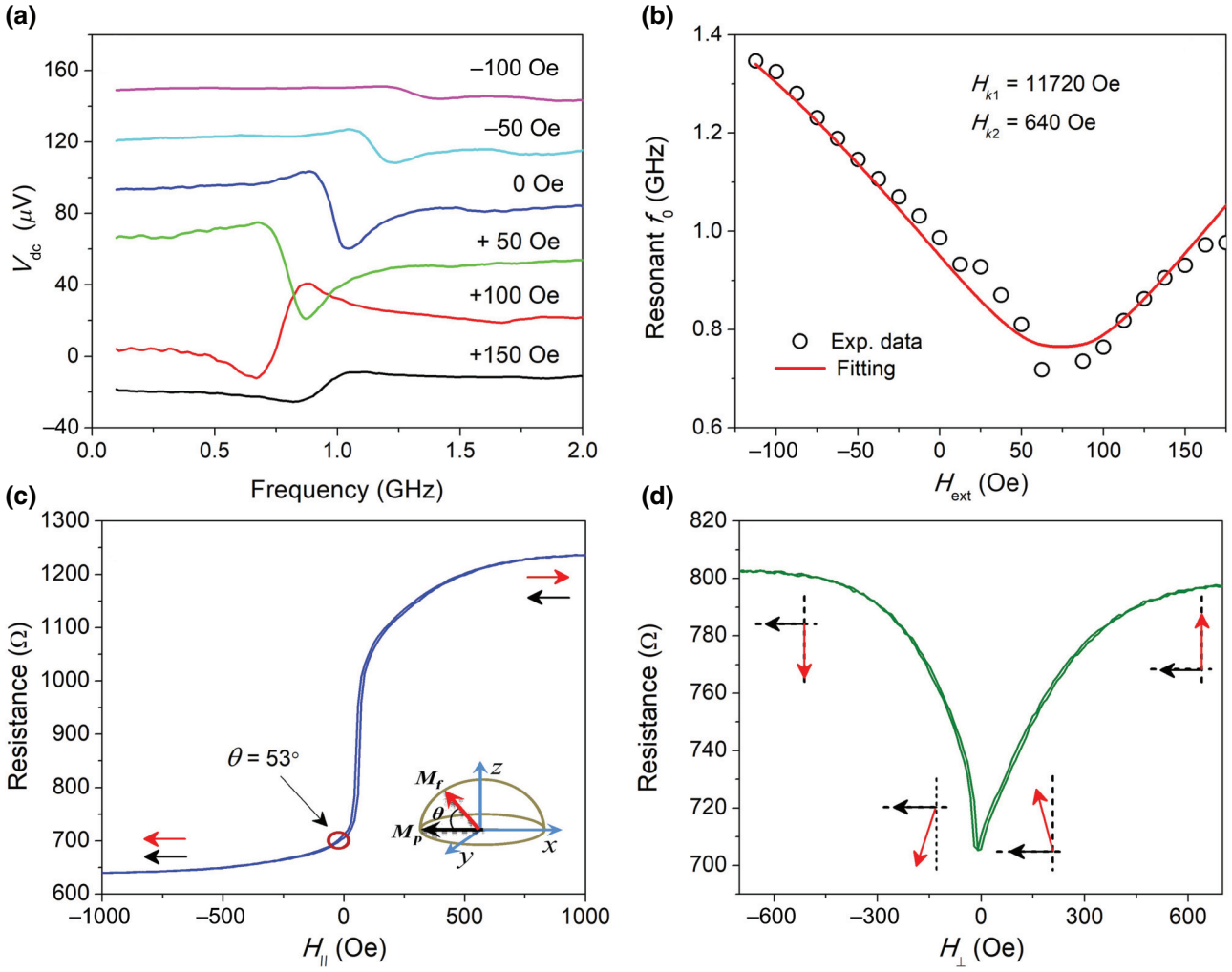

FIG. 2. (a) Rectified voltage (V_{dc}) as a function of microwave frequency for various in-plane magnetic fields. (b) A comparison between the experimental data extracted from panel (a) (black circles) and the analytical expression of the resonance frequency f_0 vs H_{ext} (red line). (c),(d) Magnetoresistance-field curves of one typical MTJ device under in-plane magnetic fields ($H_{||}$) and perpendicular magnetic fields ($H_\perp$) for $I_{dc} = 10$ μA, respectively. The resistance scan as a function of the out-of-plane and in-plane fields indicates that the free layer is canted. The inset in (a) shows the Cartesian coordinate system and the direction of the magnetization vectors. The black (red) arrow denotes the magnetization direction of the reference (free) layer.

field. The canted easy axis with an equilibrium angle (θ) at zero bias field can be computed from the field scans as described in Ref. [9] (the estimated one for our sample is 53°):

$$R^{-1}(\theta) = \frac{R_P^{-1} + R_{AP}^{-1}}{2} + \frac{R_P^{-1} - R_{AP}^{-1}}{2}\cos(\theta), \qquad (1)$$

where the resistances in the parallel (R_P) and antiparallel (R_{AP}) configurations are 640 and 1236 Ω, respectively. For the device presented here, the tunnel magnetoresistance ratio, defined as (R_{AP}-R_P)/R_P is 93%. Micromagnetic simulations also prove that the canted state is in a single domain configuration (see Supplementary Note 1 [27]).

C. Rectification properties

Next, we measure the rectified voltage with a radio frequency (rf) current in the absence of an applied magnetic field. As shown in Fig. 1(b), the rf current, $I_{ac}\sin(2\pi f_{ac}t)$, is applied to the device through a bias tee using a signal generator (N5183B, Keysight), while the rectification voltage V_{dc} across the MTJ is recorded with a nanovoltmeter (K2182, Keithley). Our results show that the frequency response of the NSD exhibits two qualitatively different behaviors as a function of the input power level:

(a) **Resonant detection**: For a relatively low incident rf power, $P_{rf} = 0.1$ μW, a resonant-type response is observed with a maximum near the FMR frequency of 1.1 GHz

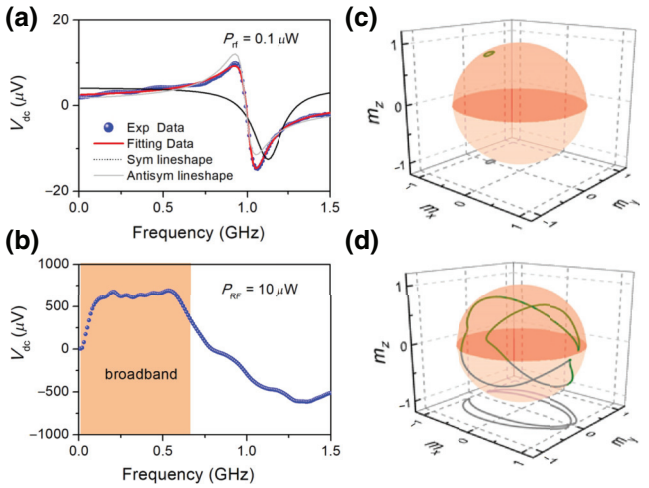

FIG. 3. (a),(b) Generated voltage (V_{dc}) as a function of rf frequency for rf powers (P_{rf}) of 0.1 and 10 μW. (c),(d) The simulated trajectories of the free-layer magnetization at $P_{rf} = 0.1$ μW and 10 μW, respectively.

[Fig. 3(a)]. The line shape associated with this peak in voltage can be fitted by a sum of symmetric and antisymmetric Lorentzian functions, as discussed in previous studies [19–21,29,30]. The origin of the asymmetric line shape is related to the voltage-controlled interfacial perpendicular magnetic anisotropy effect [21], estimated as 0.57 kOe/V for this device (See Supplementary Fig. 2 [27]).

(b) **Broadband detection**: For larger input rf power, an alternative type of broadband response is achieved. Figure 3(b) displays an example with a rf input power of $P_{rf} = 10$ μW, showing that the NSD rectifies a nearly constant voltage across a 100 to 550 MHz range. Other fabricated NSDs showed qualitatively similar results with different bandwidths and output voltages, with the widest bandwidth approaching 1.2 GHz (see Supplementary Note 2 [27]). We have also found that the broadband detection is achieved mainly for devices having an equilibrium angle (θ) at zero field between 45° and 55°.

The transition from resonant detection to broadband detection can be understood in terms of the evolution of the precession orbit [12]. At low P_{rf}, a small-amplitude magnetization precession is excited where the magnetization oscillates in a circular trajectory confined in the potential well near the equilibrium axis as shown in Fig. 3(c) [see also Video 1]. When P_{rf} is sufficiently large, the free layer oscillation becomes a large-amplitude magnetization precession [Fig. 3(d) and Video 2], and as such, results in a large rectified voltage. In the broadband region, a change of input frequency does not change the magnetization precession amplitude in the x direction, thus the rectification voltage remains nearly independent of the input frequency [Fig. 3(b)]. Similarly, the rectification voltages are approximately independent of the P_{rf} value after it exceeds a threshold [12], because the x component of the magnetization oscillates near the maximum amplitude [see the projection in the x-y plane in Fig. 3(d)], whereas additional input power is then converted to the excitation of higher nonlinear modes and does not contribute to the rectified voltage. This transition is qualitatively different from the one already observed in other spintronics diodes where, as the input power increases, only a nonlinear FMR with a strongly asymmetric line shape is excited [for an example, see Fig. 3(a) in Ref. [18]]. A quantitative comparison of our data with the model of Ref. [12] cannot be done because the trajectory of the magnetization is not circular as shown by micromagnetic simulations [see Fig. 3(d)].

Figure 4(a) displays the rectification curves under the different in-plane bias magnetic field at $P_{rf} = 3.2$ μW for the device presented in the main text. The application of a large enough magnetic field can result in a qualitative change of the rectification response by destroying the canted equilibrium state. However, there exists a field region where the response only changes quantitatively. For example, it can be seen that a large enough positive magnetic field (i.e., 50 to 75 Oe) applied along the opposite direction of the in-plane direction of the tilted state can lead to a qualitative change of the rectification response that is then characterized by a low-frequency tail. Micromagnetic

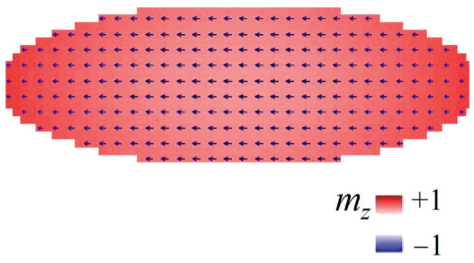

VIDEO 1. Spatial distribution of the magnetization as obtained from micromagnetic simulations when the input power is $P_{rf} = 0.1$ μW. The colors refer to the z component of the magnetization, as indicated by the color bar.

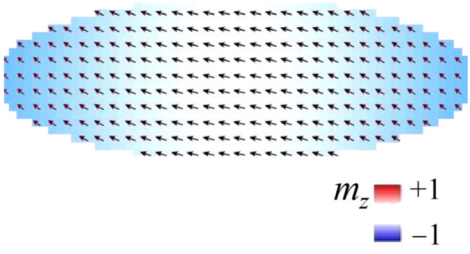

VIDEO 2. Spatial distribution of the magnetization as obtained from micromagnetic simulations when the input power is $P_{rf} = 10$ μW. The colors refer to the z component of the magnetization, as indicated by the color bar.

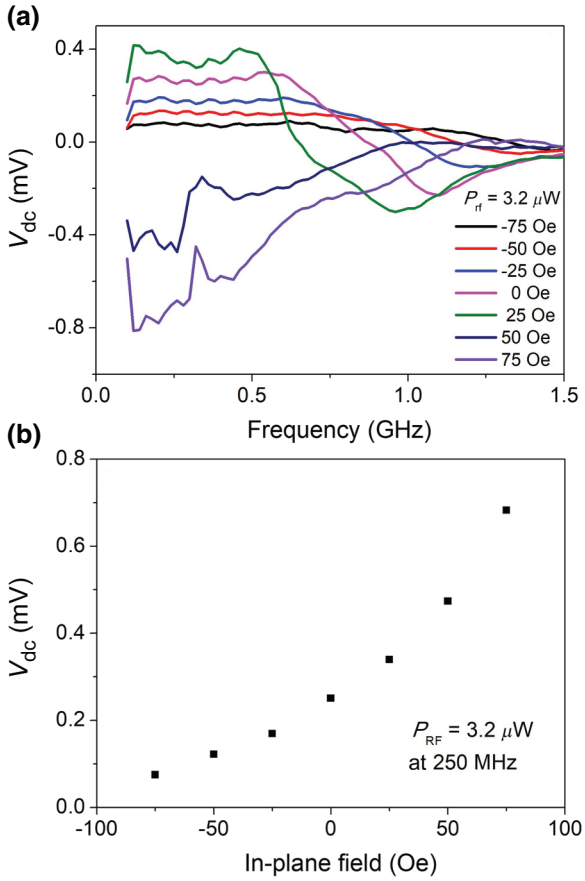

FIG. 4. (a) The rectification curve under various in-plane magnetic fields at rf input of 3.2 μW. The magnetic field is applied along the long axis of the elliptical nanopillar (positive fields are parallel to the in-plane component of the magnetization of the canted equilibrium state). (b) The amplitude of the rectified voltage as a function of the in-plane field fields at an incident rf power of 3.2 μW with 250 MHz.

simulations show that this qualitative change occurs when the equilibrium configuration of the magnetization is along the field direction. In other words, the tilted state is no longer stable. For negative fields, the broadband frequency detection exhibits only quantitative changes as compared with the one near the zero magnetic field. In particular, at 25 Oe, the detection conversion is also better than the one at zero field, but the frequency band of detection is narrower. These data show that that the field can play a role in the optimization of the broadband detection properties.

Figure 4(b) shows that the rectified voltage has a monotonic trend as a function of the in-plane field amplitude. Predictions from the theory developed in Ref. [12] of the main text show that the larger the angle (near the device plane), the larger is the trajectory that the magnetization can achieve, and hence, the larger is the rectified voltage. Micromagnetic simulations, as well as experimental data, confirm this trend. In other words, when the equilibrium axis is far from the out-of-plane axis, but still

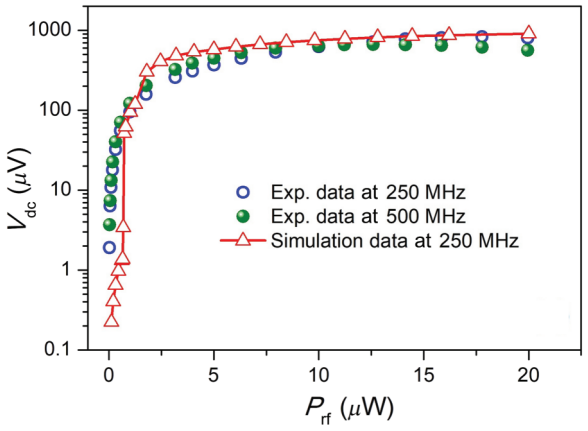

FIG. 5. A comparison of experimental and simulated data of the rectification voltage as a function of input power. The circles are the experimental data obtained at input frequencies $f_{ac} = 250$ and 500 MHz, respectively. The triangles are the simulation data at an input frequency $f_{ac} = 250$ MHz.

tilted, a more circular trajectory is excited. Therefore, the energy transferred to the higher harmonics is smaller, but the large-amplitude dynamics can follow the input up to smaller frequency values. The broadband response is more sensitive to the field applied along the out-of-plane direction because the angle of the canted state is more sensitive to this field.

Figure 5 shows the experimental performance of the device at two frequencies, 250 and 500 MHz, with the input rf power varied across a considerable energy range. The nonresonant character emerges from input powers larger than 0.53 μW, however, the generated voltages are almost constant when the input power P_{rf} is above 8 μW. This saturation mechanism is analogous to the one observed in ST oscillators at a large enough bias current [31,32]. However, those measurements clearly demonstrate that spintronic electromagnetic energy harvesters are already able to work at input powers below 1 μW.

The experimentally observed behavior is well reproduced by micromagnetic computations [33–38] (see Supplementary Note 1 [27]) as shown in Fig. 5. In conclusion, in the broadband detection scheme, the NSD operates as a nonresonant broadband microwave detector for low-frequency rf signals. The NSD is expected to be used for ultralow power detection (<10 μW) [17], hence we need to compare the NSD performance with that of the low Schottky barrier diodes [17].

D. A comparison with Schottky diodes

Supplementary Note 3 [27] shows the measurements for characterization of the state of the Schottky diode. We believe that the best metrics for this comparison are the conversion efficiency and the conversion efficiency

density [15], defined as the ratio between the conversion efficiency η_C (%) [16] and the area occupancy (AO) of the device, which is around 7.5×10^{-3} μm^2 for the NSD and larger than 10 μm^2 for the Schottky diode (SMS7630). We compute the η_C as the ratio between the dc power (P_{dc}) and the input rf power (P_{rf}), where P_{dc} is approximately given by V_{dc}^2/R_{ZBR} (V_{dc} is the rectified dc voltage and R_{ZBR} is the zero-bias resistance, 770 Ω for the broadband spintronic diode and approximately 5000 Ω for the SMS7630 Schottky diode, respectively).

Figure 6(a) shows a comparison of the performance of a single device in terms of η_C. It can be seen that the single device performance of the broadband spintronic diode (input power larger than 0.53 μW) has a smaller conversion efficiency than do the Schottky diodes (SMS7630). On the other hand, if we consider the resonant response of a single spintronic diode, the conversion efficiency turns out to be higher than that of the Schottky diode for an input power level down to nW [17].

These results are shown in Fig. 6(a), which includes the conversion efficiency at the FMR frequency of (i) a NSD used in our previous work exhibiting a large sensitivity of about 1 kV/W at zero dc bias [10], and (ii) the device studied in this work for input powers smaller than 0.53 μW. Those data, together with the fact that the theoretically predicted η_C can be as large as 3.5% [12], suggest that there is room to further improve the conversion efficiency for the broadband detection. In particular, the two challenges to face are the reduction of the threshold power toward the nW level and the increasing of the conversion efficiency for a single device. Figure 6(b) summarizes the conversion efficiency density calculated for the Schottky diode and the NSD working in the broadband region at an input frequency of 500 MHz. As can be clearly observed, the spintronic energy harvester already exhibits a better performance in terms of η_C(%)/AO as compared to the Schottky diodes. For example, this areal scaling could be important if the devices are used in a radiation-coupled (cavity or antenna at a focal point) configuration, or if the rectification occurs with an array of NSDs connected in parallel (where the dc output voltage remains the same while the equivalent resistance is reduced, thus permitting better impedance matching with the antenna and larger delivered power over a load).

Moreover, there are two more technical advantages of the NSDs: (i) they can work in a broader range of temperature and (ii) they are radiation hardened, hence, they can be used for aerospace applications.

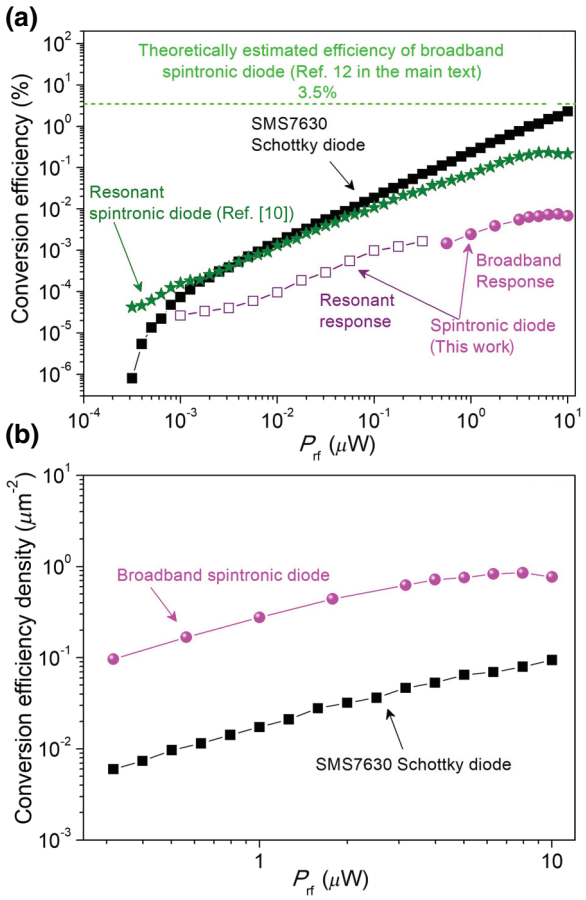

FIG. 6. (a) A comparison of rf-to-dc conversion efficiency for Schottky diodes and spintronic diodes. The efficiencies in the Schottky diodes are calculated from the rectified dc voltages at 500 MHz. The efficiency in the resonant spintronic diode (Ref. [10]) is calculated from the rectified dc voltages at the resonant frequency of 1.2 GHz. The efficiency of spintronic diode (this work) is calculated from the rectified dc voltages at 500 MHz. Below 0.53 μW, the broadband response is converted into a resonant response and the empty squares represent the conversion efficiency computed at the resonant frequency (1 GHz) for that region. The theoretically estimated efficiency of the broadband spintronic diode is adapted from Ref. [12]. (b) A comparison of the power conversion efficiency density between the Schottky diode and the NSD. The values are calculated as conversion efficiency divided by the AO of the device. The AOs of Schottky diodes and spintronic diodes are 10 and 7.5×10^{-3} μm^2, respectively.

III. NANOSCALE SPINTRONIC DIODES AS A POWER SOURCE

We now prove that the NSD can deliver a large enough power to work as a power source for a real-world circuit. Figure 7(a) shows the measurement setup. The NSD energy harvester is connected to the drain of a high-performance few-layers BP nanodevice, chosen for its low-power operating capability [39,40]. The NSD supplies the voltage (V_{ds}) by converting energy that it receives from rf sources through an antenna. Three different rf sources are used in the experiment: (i) a signal generator, (ii) a walkie-talkie, and (iii) a radiophone. Figure 7(b) shows the current I_{ds} as a function of V_{ds} where rf energy is harvested by the NSD from the signal generator. The linear I_{ds}-V_{ds} curve

shows that the NSD can be used to bias the nanodevice. Our results are now extended to consider different sources that can give rise to ambient background rf energy. We have found that a rectified dc voltage is observed when a walkie-talkie (462 MHz) or a radiophone (923 MHz) is turned on near the antenna connected to the NSD. As an example, as displayed in Fig. 7(c) for sample no. S2 (See Supplementary Fig. 2 [27]), for a 6.3-μW walkie-talkie and a 4.0-μW radiophone input rf power received through the antenna, voltages of 150 and 100 μV are measured, respectively.

Another key benefit of this NSD is that it provides rectification of more rf sources, which act simultaneously. Figure 7(d) shows an example under two rf sources. A key

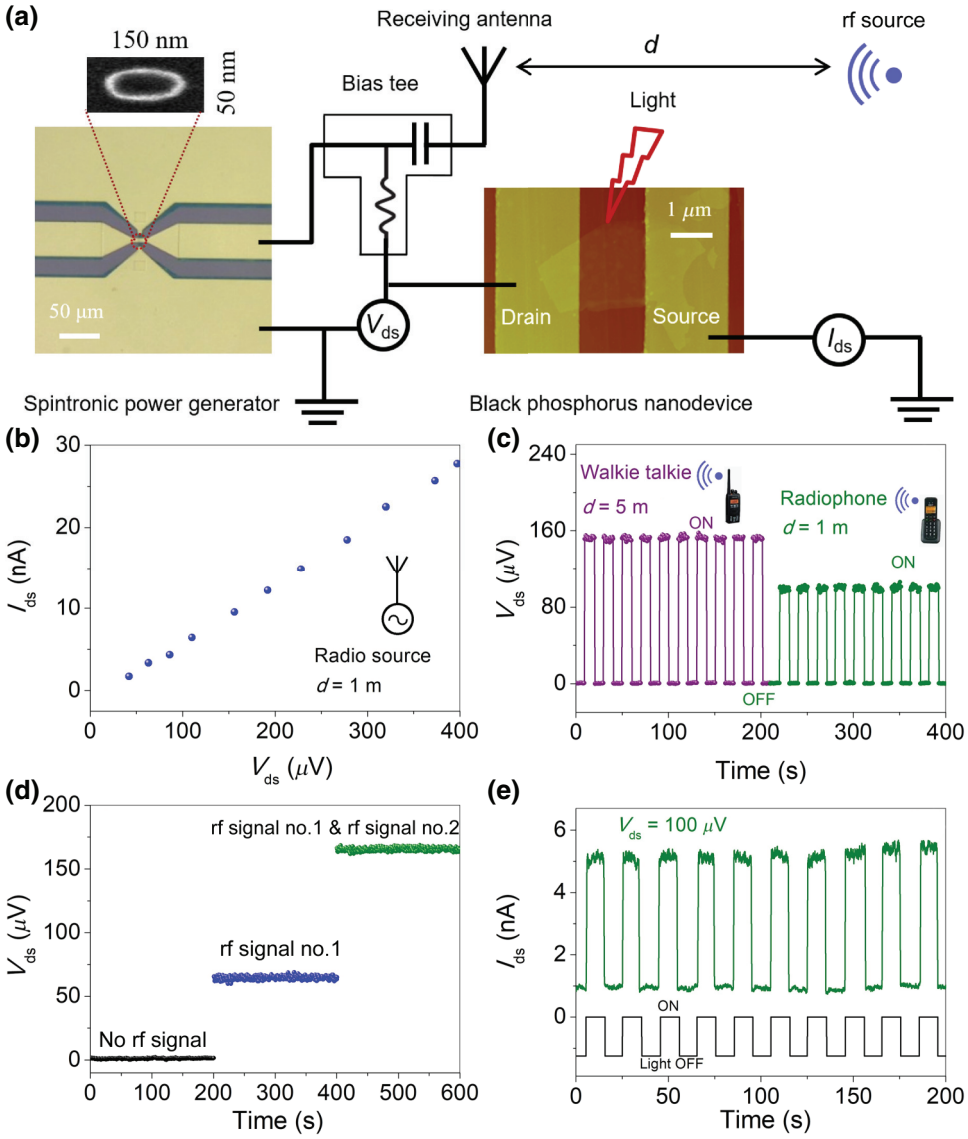

FIG. 7. (a) Schematic diagram of the self-powered circuit: the drain-source supply for the BP nanodevice is provided by the NSD power generator. The left shows the optical image of the spintronic generator with a SEM image of the MTJ nanopillar, while the right shows the AFM image of the fabricated few-layers BP nanodevice where d stands for the distance between the antenna and the rf source. (b) Powering the drain-source terminal of the BP nanodevice with the NSD device [27] (sample no. S2 in Supplementary Fig. 4) under rf energy (500 MHz) provided by a signal generator. The graph shows the current-voltage characteristics. (c) Rectified dc voltages generated by rf signals that are produced by the walkie-talkie and the radiophone, respectively. (d) Rectified dc voltages as a function of time under the simultaneous action of two signals produced by the external rf sources: rf signal no. 1 (signal generator) with a frequency of 650 MHz and a power of 3.2 μW; rf signal no. 2 (radiophone) with a frequency of 923 MHz and a power of 4.0 μW (receiving antenna terminal). The data clearly demonstrate that the broadband frequency response of the NSD device allows one to accumulate power from different rf energy sources. (e) Photoresponse of the BP transistor under light illumination at a voltage bias of 100 μV produced by the NSD that received the rf energy from the radiophone.

finding here is that the rectified dc voltage when the two external rf sources of different frequencies are acting on the NSD device simultaneously is comparable to the sum of the rectified dc voltage achieved when only one rf source is applied.

Furthermore, we consider an example of how an NSD can be used as a power supply for a BP device acting as a photosensor. The NSD provides the bias voltage while the BP acts as a sensor of photons and can be triggered by a typical light source. Figure 7(e) shows the response of this BP sensor to a modulated light when the sensor is biased by a voltage of 100 μV produced by the NSD that is harvesting the radiophone rf energy. When the light turns on, the BP enters the on-state and the resistance drops, allowing I_{ds} to increase to 5 nA. On the other hand, when the light turns off, the BP enters the off-state and the resistance increases, lowering I_{ds} to 1 nA. This phenomenon is consistent with a previous report on BP photodetection [41].

IV. SUMMARY AND CONCLUSIONS

In summary, we have experimentally demonstrated that spintronic diodes based on MTJs with canted free layers can act as nanoscale electromagnetic energy harvesters, opening a new direction for research in nanoscale spintronic energy harvesters. Our results also demonstrate that the power generated by NSDs is sufficient to drive active devices, such as BP nanosized photosensors, for use in low-power electronic systems, showing their potential as building blocks of self-powering devices for applications in biomedical applications [42], in wireless sensing, and portable electronics in the emerging era of the "internet of things."

ACKNOWLEDGMENTS

This work was supported the executive programme of scientific and technological cooperation between Italy and China funded by Ministero degli Affari Esteri e della Cooperazione Internazionale and the Minister Of Science and Technology of China of the People's Republic of China (Grants No. CN16GR09 and No. 2016YFE0104100) and by the National Science Foundation of China (Grants No. 11474311 and No. 11804370). The work at the Oakland University was in part supported by the National Science Foundation of the USA (Grants No. EFMA-1641989 and No. ECCS-1708982), by a grant from DARPA, and by a grant from the Center for NanoFerroic Devices (CNFD) and Nanoelectronics Research Initiative (NRI). The work at UCLA was supported by the Nanoscale Engineering Research Centre on Translational Applications of Nanoscale Multiferroic Systems (TANMS). R.T. also thanks the project "ThunderSKY" funded from the Hellenic Foundation for Research and Innovation (HFRI) and the General Secretariat for Research and Technology (GSRT) under Grant No. 871.

[1] S. A. Wolf, D. D. Awschalom, R. A. Buhrman, J. M. Daughton, S. von Molnár, M. L. Roukes, A. Y. Chtchelkanova, and D. M. Treger, Spintronics: A spin-based electronics vision for the future, Science **294**, 1488 (2001).

[2] I. Žutić, J. Fabian, and S. Das Sarma, Spintronics: Fundamentals and applications, Rev. Mod. Phys. **76**, 323 (2004).

[3] A. Brataas, A. D. Kent, and H. Ohno, Current-induced torques in magnetic materials, Nat. Mater. **11**, 372 (2012).

[4] N. Locatelli, V. Cros, and J. Grollier, Spin-torque building blocks, Nat. Mater. **13**, 11 (2013).

[5] S. I. Kiselev, J. C. Sankey, I. N. Krivorotov, N. C. Emley, R. J. Schoelkopf, R. a Buhrman, and D. C. Ralph, Microwave oscillations of a nanomagnet driven by a spin-polarized current, Nature **425**, 380 (2003).

[6] A. A. Tulapurkar, Y. Suzuki, A. Fukushima, H. Kubota, H. Maehara, K. Tsunekawa, D. D. Djayaprawira, N. Watanabe, and S. Yuasa, Spin-torque diode effect in magnetic tunnel junctions, Nature **438**, 339 (2005).

[7] K. Uchida, S. Takahashi, K. Harii, J. Ieda, W. Koshibae, K. Ando, S. Maekawa, and E. Saitoh, Observation of the spin Seebeck effect, Nature **455**, 778 (2008).

[8] G. E. W. Bauer, E. Saitoh, and B. J. van Wees, Spin caloritronics, Nat. Mater. **11**, 391 (2012).

[9] S. Miwa, S. Ishibashi, H. Tomita, T. Nozaki, E. Tamura, K. Ando, N. Mizuochi, T. Saruya, H. Kubota, K. Yakushiji, T. Taniguchi, H. Imamura, A. Fukushima, S. Yuasa, and Y. Suzuki, Highly sensitive nanoscale spin-torque diode, Nat. Mater. **13**, 50 (2014).

[10] B. Fang, M. Carpentieri, X. Hao, H. Jiang, J. A. Katine, I. N. Krivorotov, B. Ocker, J. Langer, K. L. Wang, B. Zhang, B. Azzerboni, P. K. Amiri, G. Finocchio, and Z. Zeng, Giant spin-torque diode sensitivity in the absence of bias magnetic field, Nat. Commun. **7**, 11259 (2016).

[11] A. S. Jenkins, R. Lebrun, E. Grimaldi, S. Tsunegi, P. Bortolotti, H. Kubota, K. Yakushiji, A. Fukushima, G. de Loubens, O. Klein, S. Yuasa, and V. Cros, Spin-torque resonant expulsion of the vortex core for an efficient radiofrequency detection scheme, Nat. Nanotechnol. **11**, 360 (2016).

[12] O. V. Prokopenko, I. N. Krivorotov, E. Bankowski, T. Meitzler, S. Jaroch, V. S. Tiberkevich, and A. N. Slavin, Spin-torque microwave detector with out-of-plane precessing magnetic moment, J. Appl. Phys. **111**, 123904 (2012).

[13] S. Ikeda, K. Miura, H. Yamamoto, K. Mizunuma, H. D. Gan, M. Endo, S. Kanai, J. Hayakawa, F. Matsukura, and H. Ohno, A perpendicular-anisotropy CoFeB–MgO magnetic tunnel junction, Nat. Mater. **9**, 721 (2010).

[14] P. Khalili Amiri, Z. M. Zeng, J. Langer, H. Zhao, G. Rowlands, Y. J. Chen, I. N. Krivorotov, J. P. Wang, H. W. Jiang, J. A. Katine, Y. Huai, K. Galatsis, and K. L. Wang, Switching current reduction using perpendicular anisotropy in CoFeB-MgO magnetic tunnel junctions, Appl. Phys. Lett. **98**, 112507 (2011).

[15] S. Priya and D. J. Inman, *Energy Harvesting Technologies* (Springer US, Boston, MA, 2009).

[16] S. Hemour and K. Wu, Radio-frequency rectifier for electromagnetic energy harvesting: Development path and future outlook, Proc. IEEE **102**, 1667 (2014).
[17] S. Hemour, Y. Zhao, C. H. P. Lorenz, D. Houssameddine, Y. Gui, C.-M. Hu, and K. Wu, Towards low-power high-efficiency RF and microwave energy harvesting, IEEE Trans. Microw. Theory Tech. **62**, 965 (2014).
[18] J. C. Sankey, P. M. Braganca, A. G. F. Garcia, I. N. Krivorotov, R. A. Buhrman, and D. C. Ralph, Spin-Transfer-Driven Ferromagnetic Resonance of Individual Nanomagnets, Phys. Rev. Lett. **96**, 227601 (2006).
[19] J. C. Sankey, Y.-T. Cui, J. Z. Sun, J. C. Slonczewski, R. A. Buhrman, and D. C. Ralph, Measurement of the spin-transfer-torque vector in magnetic tunnel junctions, Nat. Phys. **4**, 67 (2008).
[20] H. Kubota, A. Fukushima, K. Yakushiji, T. Nagahama, S. Yuasa, K. Ando, H. Maehara, Y. Nagamine, K. Tsunekawa, D. D. Djayaprawira, N. Watanabe, and Y. Suzuki, Quantitative measurement of voltage dependence of spin-transfer torque in MgO-based magnetic tunnel junctions, Nat. Phys. **4**, 37 (2008).
[21] J. Zhu, J. A. Katine, G. E. Rowlands, Y.-J. Chen, Z. Duan, J. G. Alzate, P. Upadhyaya, J. Langer, P. K. Amiri, K. L. Wang, and I. N. Krivorotov, Voltage-Induced Ferromagnetic Resonance in Magnetic Tunnel Junctions, Phys. Rev. Lett. **108**, 197203 (2012).
[22] T. Nozaki, Y. Shiota, S. Miwa, S. Murakami, F. Bonell, S. Ishibashi, H. Kubota, K. Yakushiji, T. Saruya, A. Fukushima, S. Yuasa, T. Shinjo, and Y. Suzuki, Electric-field-induced ferromagnetic resonance excitation in an ultrathin ferromagnetic metal layer, Nat. Phys. **8**, 491 (2012).
[23] S. S. P. Parkin, C. Kaiser, A. Panchula, P. M. Rice, B. Hughes, M. Samant, and S.-H. Yang, , Giant tunnelling magnetoresistance at room temperature with MgO (100) tunnel barriers, Nat. Mater. **3**, 862 (2004).
[24] S. Yuasa, T. Nagahama, A. Fukushima, Y. Suzuki, and K. Ando, Giant room-temperature magnetoresistance in single-crystal Fe/MgO/Fe magnetic tunnel junctions, Nat. Mater. **3**, 868 (2004).
[25] M. Tarequzzaman, A. S. Jenkins, T. Böhnert, J. Borme, L. Martins, E. Paz, R. Ferreira, and P. P. Freitas, Broadband voltage rectifier induced by linear bias dependence in CoFeB/MgO magnetic tunnel junctions, Appl. Phys. Lett. **112**, 252401 (2018).
[26] Z. Zeng, G. Finocchio, B. Zhang, P. K. Amiri, J. A. Katine, I. N. Krivorotov, Y. Huai, J. Langer, B. Azzerboni, K. L. Wang, and H. Jiang, Ultralow-current-density and bias-field-free spin-transfer nano-oscillator, Sci. Rep. **3**, 1426 (2013).
[27] Supplemental Material, can be found at http://link.aps.org/supplemental/10.1103/PhysRevApplied.0.XXXXXX for a detailed description of the micromagnetic model, estimation of the VCMA, experimental data from additional devices with canted free layer, and the characterization of the Schottky diodes.
[28] Z. Zeng, K. H. Cheung, H. W. Jiang, I. N. Krivorotov, J. A. Katine, V. Tiberkevich, and A. Slavin, Evolution of spin-wave modes in magnetic tunnel junction nanopillars, Phys. Rev. B **82**, 100410 (2010).
[29] C. Wang, Y.-T. Cui, J. Z. Sun, J. A. Katine, R. A. Buhrman, and D. C. Ralph, Bias and angular dependence of spin-transfer torque in magnetic tunnel junctions, Phys. Rev. B **79**, 224416 (2009).
[30] M. Harder, Y. Gui, and C.-M. Hu, Electrical detection of magnetization dynamics via spin rectification effects, Phys. Rep. **661**, 1 (2016).
[31] G. Finocchio, G. Siracusano, V. Tiberkevich, I. N. Krivorotov, L. Torres, and B. Azzerboni, Time-domain study of frequency-power correlation in spin-torque oscillators, Phys. Rev. B **81**, 184411 (2010).
[32] V. E. Demidov, M. Evelt, V. Bessonov, S. O. Demokritov, J. L. Prieto, M. Muñoz, J. Ben Youssef, V. V. Naletov, G. de Loubens, O. Klein, M. Collet, P. Bortolotti, V. Cros, and A. Anane, Direct observation of dynamic modes excited in a magnetic insulator by pure spin current, Sci. Rep. **6**, 32781 (2016).
[33] G. Finocchio, B. Azzerboni, G. D. Fuchs, R. A. Buhrman, and L. Torres, Micromagnetic modeling of magnetization switching driven by spin-polarized current in magnetic tunnel junctions, J. Appl. Phys. **101**, 063914 (2007).
[34] M. Carpentieri, R. Tomasello, S. Vergura, F. Garesci, G. Siracusano, M. D'Aquino, and G. Finocchio, Micromagnetic analysis of statistical switching in perpendicular magnetic tunnel junctions with double reference layers, IEEE Magn. Lett. **9**, 3102105 (2018).
[35] J. C. Slonczewski, Currents, torques, and polarization factors in magnetic tunnel junctions, Phys. Rev. B **71**, 024411 (2005).
[36] J. C. Slonczewski and J. Z. Sun, Theory of voltage-driven current and torque in magnetic tunnel junctions, J. Magn. Magn. Mater. **310**, 169 (2007).
[37] G. Siracusano, R. Tomasello, A. Giordano, V. Puliafito, B. Azzerboni, O. Ozatay, M. Carpentieri, and G. Finocchio, Magnetic Radial Vortex Stabilization and Efficient Manipulation Driven by the Dzyaloshinskii-Moriya Interaction and Spin-Transfer Torque, Phys. Rev. Lett. **117**, 087204 (2016).
[38] G. Finocchio, M. Ricci, R. Tomasello, A. Giordano, M. Lanuzza, V. Puliafito, P. Burrascano, B. Azzerboni, and M. Carpentieri, Skyrmion based microwave detectors and harvesting, Appl. Phys. Lett. **107**, 262401 (2015).
[39] L. Li, Y. Yu, G. J. Ye, Q. Ge, X. Ou, H. Wu, D. Feng, X. H. Chen, and Y. Zhang, Black phosphorus field-effect transistors, Nat. Nanotechnol. **9**, 372 (2014).
[40] B. Yang, B. Wan, Q. Zhou, Y. Wang, W. Hu, W. Lv, Q. Chen, Z. Zeng, F. Wen, J. Xiang, S. Yuan, J. Wang, B. Zhang, W. Wang, J. Zhang, B. Xu, Z. Zhao, Y. Tian, and Z. Liu, Te-doped black phosphorus field-effect transistors, Adv. Mater. **28**, 9408 (2016).
[41] M. Buscema, D. J. Groenendijk, S. I. Blanter, G. A. Steele, H. S. J. van der Zant, and A. Castellanos-Gomez, Fast and broadband photoresponse of few-layer black phosphorus field-effect transistors, Nano Lett. **14**, 3347 (2014).
[42] J. R. Choi, K. W. Yong, J. Y. Choi, A. Nilghaz, Y. Lin, J. Xu, and X. Lu, Black phosphorus and its biomedical applications, Theranostics **8**, 1005 (2018).